Viscous Overstability in Saturn's B-Ring

II. Hydrodynamic Theory and Comparison to Simulations

Jürgen Schmidt

Institute of Physics, Department of Nonlinear Dynamics, University of Potsdam, D-14415 Potsdam, Germany
E-mail: jschmidt@agnld.uni-potsdam.de

Heikki Salo

Department of Physical Sciences, Division of Astronomy, University of Oulu, Finland

and

Frank Spahn and Olaf Petzschmann

Institute of Physics, Department of Nonlinear Dynamics, University of Potsdam, D-14415 Potsdam, Germany

We investigate the viscous oscillatory instability (overstability) of an unperturbed dense planetary ring, an instability that might play a role in the formation of radial structure in Saturn's B-ring. We generalize existing hydrodynamic models by including the heat flow equation in the analysis and compare our results to the development of overstable modes in local particle simulations. With the heat flow, in addition to the balance equations for mass and momentum, we take into account the balance law for the energy of the random motion; i.e., we allow for a thermal mode in a stability analysis of the stationary Keplerian flow. We also incorporate the effects of nonlocal transport of momentum and energy on the stability of the ring. In a companion paper (Salo, H., J. Schmidt, and F. Spahn 2001. *Icarus*, doi:10.1006/icar.2001.6680) we describe the determination of the local and nonlocal parts of the viscosity, the heat conductivity, the pressure, as well as the collisional cooling, together with their dependences on temperature and density, in local event-driven simulations of a planetary ring. The ring's self-gravity is taken into account in these simulations by an enhancement of the frequency of vertical oscillations $\Omega_z > \Omega$. We use these values as parameters in our hydrodynamic model for the comparison to overstability in simulated rings of meter-sized inelastic particles of large optical depth with $\Omega_z/\Omega = 3.6$. We find that the inclusion of the energy-balance equation has a stabilizing influence on the overstable modes, shifting the stability boundary to higher optical depths, and moderating the growth rates of the instability, as compared to a purely isothermal treatment. The non-isothermal model predicts correctly the growth rates and oscillation frequencies of overstable modes in the simulations, as well as the phase shifts and relative amplitudes of the perturbations in density and radial and tangential velocity. © **2001 Academic Press**

Key Words: planetary rings; Saturn.

1. INTRODUCTION

The Voyager missions revealed a pronounced radial structure of the B-ring and the inner A-ring of Saturn appearing on a wide range of length scales down to the resolution limit of the Voyager observations (Smith *et al.* 1982; Esposito *et al.* 1983a,b). Several explanations for the formation of the structure have been proposed in the literature. Besides the interaction of embedded moonlets with the ring particles (Lissauer *et al.* 1981; Hénon 1981; Spahn and Sponholz 1989), at least part of the structure was attributed to the dynamics of charged grains and the associated radial momentum transport (Goertz and Morfill 1988) and to ballistic transport (Durisen 1995). Lukkari (1981), Lin and Bodenheimer (1981) and Ward (1981) suggested a viscous instability of the particle flow to be responsible for the structure. This is a diffusive instability that takes place when $d(\nu\sigma)/d\sigma$ is negative, where ν is the kinematic viscosity and σ is the surface density. However, in theoretical models (Araki and Tremaine 1986) this derivative is found to be large and positive rather than negative, in accordance with numerical simulations (Wisdom and Tremaine 1988; Salo 1991, 1992b). In addition, no signs of a viscous instability have been found in the latter simulations. The theoretically and numerically observed density dependence of the kinematic viscosity, however, allows for the so-called viscous overstability, investigated in accretion disks (Kato 1978; Blumenthal *et al.* 1984) and in the context of planetary rings (Borderies *et al.* 1985; Papaloizou and Lin 1988; Schmit and Tscharnuter 1995; Mosqueira 1996). Here, the restoring forces after a small perturbation are directed back to equilibrium but are so strong that the system overshoots the position at the other side of

equilibrium.[1] The hydrodynamic picture of this process is a wave with growing amplitude. Such a behavior is indeed observed in direct N-particle simulations (see Salo *et al.* 2001) of dense self-gravitating planetary rings for various particle-sizes and internal particle-densities, different models for the inelasticity of the collisions, and for different ways of simulating the particles' self-gravity. In this paper we give a quantitative comparison between the overstability of a hydrodynamic model ring and the simulations.

In a recent paper (Spahn *et al.* 2000) we reported on the qualitative effect of the energy balance equation on the overstability in a hydrodynamic model of a vertically thin, viscous, self-gravitating, Keplerian disk. Thus, the model allowed for spatially dependent temperature variations, fulfilling the balance of collisional cooling, viscous heating, and heat flow. It is important to note that here temperature refers to the random kinetic energy of the ring particles defined by the trace of the squared velocity dispersion tensor as $T = (1/3)\textbf{Tr}\langle c_i c_j\rangle$. In the present study, we investigate the influence of the thermal mode in greater detail, using transport coefficients and values for the pressure and collisional cooling that have been determined in event-driven local simulations (Salo *et al.* 2001).

Approximating the self-gravity by an enhancement of the frequency of vertical oscillations (Wisdom and Tremaine 1988), we find a stability boundary of $\tau \gtrsim 1$, optically thinner rings being stable. This is in agreement with the results of Mosqueira (1996) who simulated perturbed states of a dense planetary ring and found that the criterion for viscous overstability given by Borderies *et al.* (1985) is fulfilled for parameters of the outer saturnian B-ring ($\tau \sim 1.8$) but not for the uranian ε-ring ($\tau \sim 1$).

The paper is organized as follows. In Section 2 we display the hydrodynamic balance laws of mass, momentum, and energy together with the constitutive equations for momentum and heat flux and derive the linearized equations that yield the linear instabilities of the basic stationary flow. In Section 3 we briefly discuss the time asymptotic, linear stability of non-axisymmetric perturbations and in Section 4 we derive expressions for the growth rates of the linear oscillatory instability and the linear eigenfunctions at marginal stability. In Section 5 we compare these results to data obtained from simulations, and finally in Section 6 we summarize our results and discuss the limitations and possible extensions of the model, as well as the implications to Saturn's rings.

2. THE HYDRODYNAMIC APPROXIMATION

2.1. Basic Equations

We describe the ring as a vertically thin, self-gravitating, viscous fluid disk, consisting of inelastic, uni-sized, smooth, spherical particles. The mean fields of surface density σ, velocity $\vec{u}$,

and temperature T are supposed to obey the hydrodynamic balance laws for mass, momentum, and energy. In this specific case, the last balance law contains a cooling term Γ that accounts for the steady dissipation of energy of the motion due to the inelastic collisions of the ring particles. With the pressure tensor $\hat{P}$, the heat flux vector $\vec{q}$, the gravitational force field $\vec{F}$ of the central planet, and the disk's mean-field self-gravity potential ϕ these balance equations read

$$(\partial_t + \vec{u} \cdot \vec{\nabla})\sigma = -\sigma \vec{\nabla} \cdot \vec{u}$$
$$\sigma(\partial_t + \vec{u} \cdot \vec{\nabla})\vec{u} = \sigma \vec{F} - \sigma \vec{\nabla}\phi - \vec{\nabla} \cdot \hat{P} \quad (1)$$
$$\frac{3}{2}\sigma(\partial_t + \vec{u} \cdot \vec{\nabla})T = -\hat{P} : \vec{\nabla}\vec{u} - \vec{\nabla} \cdot \vec{q} - \Gamma .$$

Here, we employ the thin-disk approximation, i.e., vertical degrees of freedom are integrated out, σ is the ring's surface density, and $\hat{P}$, $\vec{q}$, and Γ are vertically integrated quantities. The thin-disk approximation is motivated by the extremely small thickness of the saturnian rings and it is justified a posteriori by the quantitative match we achieve between the theoretical results and the simulations. Nevertheless, the dynamical consequences of the vertical degrees of freedom of the ring material on the overstability should be investigated in future models.

We express the balance equations in a Cartesian coordinate system co-rotating in the ring plane at distance r_0 from the central planet. Let x and y denote the radial and circumferential direction in that system. The linearized central gravitational force per unit mass expressed in that frame is

$$\vec{F} = 3\Omega^2 x\vec{e}_x - 2\Omega\vec{e}_z \times \vec{u} , \quad (2)$$

where $\Omega = \sqrt{GM/r_0^3}$, is the Kepler frequency at r_0. The thermodynamic fluxes of momentum ($\hat{P}$), and energy ($\vec{q}$) are related to their respective thermodynamic forces ($\vec{\nabla}\vec{u}$, $\vec{\nabla}T$) via a linear ansatz; i.e.,

$$\hat{P}_{\alpha\beta} = \delta_{\alpha\beta} p - 2\eta D_{\alpha\beta} - \delta_{\alpha\beta}\xi\nabla_\lambda u_\lambda \quad (3)$$

and

$$\vec{q} = -\kappa_D \vec{\nabla}T . \quad (4)$$

The transport coefficients η, ξ, and κ_D are the vertically integrated *dynamic* shear and bulk viscosity and the heat conductivity, respectively. $\hat{D}$ is the traceless shear tensor

$$D_{\alpha\beta} = \frac{1}{2}\left(\nabla_\alpha u_\beta + \nabla_\beta u_\alpha - \frac{2}{3}\delta_{\alpha\beta}\nabla_\lambda u_\lambda\right). \quad (5)$$

With these constitutive equations the balance laws are the continuity equation, Navier–Stokes equation, and heat-flow equation of viscous hydrodynamics, extended by the cooling function Γ, as they are used in the theory of granular matter flow (Jenkins and Richman 1985).

---

[1] It seems that the name "overstability," being somewhat counterintuitive, actually is motivated by this picture. The naming can be traced back to Sir Arthur Eddington (Chandrasekhar 1981, p. 3).

The self-gravity potential ϕ satisfies Poisson's equation

$$\nabla^2\phi = 4\pi G\sigma\delta(z), \tag{6}$$

where G is the gravitational constant and $\delta(z)$ is Dirac's delta function. A solution of this equation is (see, e.g., Binney and Tremaine 1987)

$$\phi(x, y, z) = -\frac{2\pi G}{|k|}\sigma(x, y)\exp\{-k|z|\}, \tag{7}$$

where k is the inverse of a typical length of variations of σ, which we will identify with the modulus of the wave vector of harmonic density perturbations in Section 2.2 (see also Julian and Toomre 1966; Goldreich and Tremaine 1978b). For the stability of the thin-disk this equation is of interest at $z = 0$.

Please refer to Table I for a list of symbols used in this paper.

2.2. Linear Stability

Let Σ, $\vec{U}$, and T_0 denote the state variables in the stationary state and ϕ_0 its self-gravity potential. For a local region of a planetary ring, Σ, T_0, and ϕ_0 are constants in our model. We neglect a secular, viscous inward drift of the ring particles, as well as the small influence of the planetary oblateness and the disk's self-gravity potential on the orbital frequency, and write for the velocity of the stationary state $\vec{U} = -(3/2)\Omega(r_0)x\vec{e}_y$ in the co-rotating frame. Now we allow for small perturbations σ, T, ϕ, and $\vec{u} = (u, v)$ of the stationary state. Linearizing and inserting the constitutive relations (3, 4) in Eq. (1), we obtain linearized balance equations, neglecting terms that are higher than linear order in $\sigma, T, \vec{u}$, and their derivatives. Introducing the ground state *kinematic* shear and bulk viscosity ν and ζ we find

$$\frac{D\sigma}{Dt} = -\Sigma\vec{\nabla}\cdot\vec{u}$$

$$\frac{Du}{Dt} = 2\Omega v - \frac{1}{\Sigma}\left(\frac{\partial p}{\partial\sigma}\Big|_0\frac{\partial\sigma}{\partial x} + \frac{\partial p}{\partial T}\Big|_0\frac{\partial T}{\partial x}\right) + \nu\nabla^2 u$$
$$- \frac{3\Omega}{2\Sigma}\left(\frac{\partial\eta}{\partial\sigma}\Big|_0\frac{\partial\sigma}{\partial y} + \frac{\partial\eta}{\partial T}\Big|_0\frac{\partial T}{\partial y}\right)$$
$$+ \left(\frac{\nu}{3} + \zeta\right)\frac{\partial}{\partial x}(\vec{\nabla}\cdot\vec{u}) - \frac{\partial\phi}{\partial x}$$

$$\frac{Dv}{Dt} = -\frac{1}{2}\Omega u - \frac{1}{\Sigma}\left(\frac{\partial p}{\partial\sigma}\Big|_0\frac{\partial\sigma}{\partial y} + \frac{\partial p}{\partial T}\Big|_0\frac{\partial T}{\partial y}\right) + \nu\nabla^2 v$$
$$- \frac{3\Omega}{2\Sigma}\left(\frac{\partial\eta}{\partial\sigma}\Big|_0\frac{\partial\sigma}{\partial x} + \frac{\partial\eta}{\partial T}\Big|_0\frac{\partial T}{\partial x}\right)$$
$$+ \left(\frac{\nu}{3} + \zeta\right)\frac{\partial}{\partial y}(\vec{\nabla}\cdot\vec{u}) - \frac{\partial\phi}{\partial y}$$

$$\frac{DT}{Dt} = \frac{2}{3\Sigma}\left[-P\vec{\nabla}\cdot\vec{u} - 3\eta\Omega\left(\frac{\partial v}{\partial x} + \frac{\partial u}{\partial y}\right)\right.$$
$$+ \frac{9}{4}\Omega^2\left(\frac{\partial\eta}{\partial\sigma}\Big|_0\sigma + \frac{\partial\eta}{\partial T}\Big|_0 T\right)$$
$$- \left(\frac{\partial\Gamma}{\partial\sigma}\Big|_0\sigma + \frac{\partial\Gamma}{\partial T}\Big|_0 T\right) + \left.\kappa_D\nabla^2 T\right]$$

$$\phi(r) = -\frac{2\pi G}{|k|}\sigma. \tag{8}$$

Here, $D/Dt \equiv \partial_t - \frac{3}{2}\Omega x\partial_y$ is the material derivative and the

TABLE I
List of Symbols

Symbol	Definition
R_p	Particle-radius
Σ	Uniform ground state surface density
σ	Local perturbation from ground state surface density
$\vec{U}, \vec{u}$	Ground state velocity, local perturbation velocity
u	Radial velocity perturbation
v	Tangential velocity perturbation
T_0, T	Ground state temperature (velocity dispersion), local perturbation
ϕ_0, ϕ	Ring's ground state self-gravity potential, local perturbation
τ	Optical depth
c	Effective velocity dispersion
Ω	Kepler frequency
G	Gravitational constant
$g = \frac{\pi G\Sigma}{c\Omega}$	Dimensionless gravity parameter (inverse of Toomre's parameter)
$\vec{F}$	Central gravity
$\hat{P}$	Pressure tensor
$\hat{D}$	Traceless shear tensor
$\vec{q}$	Heat flow vector
Γ	Energy dissipation due to inelastic collisions
p	Scalar pressure
η, ν	Dynamic and kinematic shear viscosity
ξ, ζ	Dynamic and kinematic bulk viscosity
κ_D, κ	Dynamic and kinematic heat conductivity
k	Modulus of radial wavenumber[a]
p_σ, p_T	Density and temperature derivative of the total pressure, taken at the ground state
η_σ, η_T	Density and temperature derivative of the dynamic shear viscosity
Γ_σ, Γ_T	Density and temperature derivative of the cooling function
$E_T = \frac{2}{3}\Gamma_T - \frac{3}{2}\eta_T$	Temperature derivative of the radial energy balance
ω	Complex growth rate of overstable modes
$\beta = \frac{\partial\log\nu}{\partial\log\sigma}$	Exponent of density dependence of the kinematic shear viscosity
s	Oscillation frequency of overstable modes near marginal stability
$\varphi_{1,2}$	Marginal eigenvectors of overstable modes

[a] In Section 3 the total wavenumber $k = \sqrt{m^2 + n^2}$ with azimuthal and radial components m and n.

symbol $|_0$ denotes that the respective differentiation is taken at the system's ground state. The perturbations in the self-gravity potential can be expressed through the perturbations in the density by use of the last equation.

We scale time with the inverse orbital frequency Ω^{-1}, density with the ground state quantity Σ, and velocities with the effective velocity dispersion c, and length is scaled by c/Ω. The effective velocity dispersion c is defined via the *total* ground state pressure as

$$p = c^2 \Sigma. \tag{9}$$

The effective velocity dispersion c deviates from the ground state velocity dispersion $\sqrt{T}$ as it includes also the effect of nonlocal pressure. In what follows, all variables and parameters are scaled quantities, their notation is unchanged. Further, we introduce the parameter $g \equiv \pi G \Sigma/(c\Omega)$, which accounts for the influence of the system's self-gravity. The parameter g is the inverse of the Toomre parameter (Toomre 1964).

$$\hat{M} = \begin{pmatrix} 0 & -i\,n & -i m & 0 \\ i\left(2\frac{g\,n}{k} - \frac{3}{2}\eta_\sigma m - p_\sigma n\right) & -\left(\nu m^2 + n^2\left(\frac{4}{3}\nu + \zeta\right)\right) & 2 - nm\left(\frac{\nu}{3} + \zeta\right) & -i\left(\frac{3}{2}\eta_T m + p_T n\right) \\ i\left(2\frac{g\,m}{k} - \frac{3}{2}\eta_\sigma n - p_\sigma m\right) & -1/2 - nm\left(\frac{\nu}{3} + \zeta\right) & -\left(\nu n^2 + m^2\left(\frac{4}{3}\nu + \zeta\right)\right) & -i\left(\frac{3}{2}\eta_T n + p_T m\right) \\ \frac{3}{2}\eta_\sigma - \frac{2}{3}\Gamma_\sigma & -i\left(2m\,\nu + \frac{2}{3}p\,n\right) & -i\left(2n\,\nu + \frac{2}{3}pm\right) & -E_T - \frac{2}{3}\kappa k^2 \end{pmatrix}. \tag{13}$$

In short, we define

$$p_\sigma \equiv \left.\frac{\partial p}{\partial \sigma}\right|_0, \qquad p_T \equiv \left.\frac{\partial p}{\partial T}\right|_0$$

for the derivatives of the total pressure (including a local and nonlocal part) and equivalent symbols for the ground state derivatives of (scaled) η and Γ. Note that p_σ does not reduce to the temperature of the system when p has a nonlocal component. Further we write

$$E_T \equiv \frac{2}{3}\left.\frac{\partial \Gamma}{\partial T}\right|_0 - \frac{3}{2}\left.\frac{\partial \eta}{\partial T}\right|_0, \tag{10}$$

describing the linear reaction of the ground state radial energy balance to variations in temperature.

We take non-axisymmetric perturbations of the stationary state (although we will focus in the stability analyses in Section 4 on purely radial perturbations) with azimuthal wavenumber m, radial wavenumber $n = l + \frac{3}{2}mt$ in shearing coordinates (see, e.g., Goldreich and Tremaine 1978b)

$$\begin{pmatrix} \sigma \\ u \\ v \\ T \end{pmatrix} = \begin{pmatrix} \sigma_t(t) \\ u_t(t) \\ v_t(t) \\ T_t(t) \end{pmatrix} \exp\left\{i\left(l + \frac{3}{2}mt\right)x + i\,my\right\}, \tag{11}$$

with time dependent amplitude functions $\sigma_t(t)$, $u_t(t)$, $v_t(t)$, $T_t(t)$. All modes with initial radial wavenumber l are "wound up" with time by differential rotation unless they have a vanishing azimuthal wavenumber m.

The solutions (11) with continuous wavenumbers describe an infinitely extended system. Periodic boundary conditions, as for example used in local simulations, require a discrete set of m and n, commensurable with a length of periodicity. In shearing coordinates the dependence of the linearized equations on the radial coordinate x is turned into a time dependence. Thus, we obtain for the amplitude functions a set of linear ordinary differential equations with time dependent coefficients

$$\begin{pmatrix} \dot{\sigma}_t \\ \dot{u}_t \\ \dot{v}_t \\ \dot{T}_t \end{pmatrix} = \hat{M}(t) \begin{pmatrix} \sigma_t \\ u_t \\ v_t \\ T_t \end{pmatrix}, \tag{12}$$

where $\hat{M}$ is the coefficient matrix that depends on time through n

Here $k \equiv \sqrt{m^2 + n^2}$ is the modulus of the wavenumber. $\hat{M}$ is the Jacobian matrix of the nonlinear Eqs. (1) in Fourier space.

3. ASYMPTOTIC LINEAR STABILITY OF NON-AXISYMMETRIC PERTURBATIONS

We derive expressions for the asymptotic (large time) behavior of the solutions to Eq. (12), following the treatment of Dubrulle and Knobloch (1992) of a similar system of equations for compressible plane Couette flow. We assume that for large times the solutions can be expressed in the form

$$\begin{pmatrix} \sigma_t \\ u_t \\ v_t \\ T_t \end{pmatrix} = \begin{pmatrix} \hat{\sigma} \\ \hat{u} \\ \hat{v} \\ \hat{T} \end{pmatrix} \exp\{\theta(t)\}. \tag{14}$$

Then $\dot{\theta}(t)$ is given by the eigenvalues of the coefficient matrix (13). Since the highest order of t in Eq. (12) is t^2 we seek for functions $\dot{\theta}(t)$ that can be expanded asymptotically as

$$\dot{\theta} = a_2 t^2 + a_1 t + a_0 + a_{-1}/t \cdots . \tag{15}$$

When we expand additionally the $1/k$ term in Eq. (12) asymptotically in powers of $1/t$ we get a sequence of eigenvalue problems (at orders $t^2, t, 1, t^{-1}, \ldots$) that yields four distinct solutions for each coefficient a_i. Inserting the a_i in Eq. (15) the corresponding four solutions for the function $\theta(t)$ are in leading order in t

$$
\begin{aligned}
\theta_1 &= -\frac{p_\sigma t}{\frac{4}{3}\nu + \zeta} + O(1) \\
\theta_2 &= -\frac{1}{2}\kappa\, m^2\, t^3 + O(t^2) \\
\theta_3 &= -\frac{3}{4}\nu\, m^2\, t^3 + O(t^2) \\
\theta_4 &= -\frac{3}{4}\left(\frac{4}{3}\nu + \zeta\right)m^2 t^3 + O(t^2).
\end{aligned}
\tag{16}
$$

Thus, all non-axisymmetric modes are *linearly* stable,[2] decaying asymptotically as $\exp\theta_i$. Every small non-axisymmetric perturbation is "wound up" by the differential rotation of the system; its radial wavelength tending eventually to zero.

The linear stability of modes with $m \neq 0$ does not mean, however, that the spontaneous formation of non-axisymmetric structure is impossible in this system. The set of equations (12) allows for transient growth of small initial fluctuations that can even grow in the nonlinear regime, thus violating the validity of the linear approximation, and may locally change the ground state considerably (Dubrulle and Knobloch 1992). In the context of the excitations of density waves in galaxies this amplification mechanism has been discussed for a similar (but non-viscid) system for instance by Julian and Toomre (1966) and Goldreich and Tremaine (1978b). In a planetary ring the gravitational interaction of non-axisymmetric structures may give rise to gravitational wakes (Salo 1992a). In Salo *et al.* (2001) we showed that in simulations such gravitational wakes in general coexist with the purely radial oscillating density pattern formed by overstable modes of axisymmetric perturbations. In this study we focus our attention on the radial structure caused by overstability, forming spontaneously from the homogeneous ground state. Thus, we investigate the case $m = 0$ of Eq. (12) in the following section in greater detail.

4. THE AXISYMMETRIC CASE

Here, we address the case $m = 0$ of Eq. (12), so that the coefficient matrix $\hat{M}$ is now independent of time. Then the time dependence of the hydrodynamic variables is of the form $\exp\{\omega t\}$ and the complex growth rates ω of infinitesimal perturbations of the ground state are given by the eigenvalues of the linearized equations in Fourier space.

4.1. Growth Rates

The characteristic equation of $\hat{M}$ for $m = 0$ yields a real local dispersion relation connecting ω and the modulus of the radial wavenumber k

$$
0 = f_0(k) + f_1(k)\omega + f_2(k)\omega^2 + f_3(k)\omega^3 + \omega^4.
\tag{17}
$$

For the kinematic shear viscosity we assume a dependence of the surface density of the form (Schmit and Tscharnuter 1995)

$$
\nu \propto \sigma^\beta.
\tag{18}
$$

The assumption of a constant β is justified for small amplitudes of the density perturbation. However, β can be varied with the ground state density Σ, thus serving as an order parameter in the analysis. The derivative of the dynamic viscosity with respect to density then reads

$$
\eta_\sigma = \nu(\beta + 1).
\tag{19}
$$

The functions f_i are given in Spahn *et al.* (2000) in terms of unscaled quantities in the notation of Eq. (8). Here, we express the dispersion relation (17) in the form

$$
\begin{aligned}
0 = p_\mathrm{T} k^2 &\left(-k^2\left(\frac{2}{3}\Gamma_\sigma \nu + \frac{3}{2}(1+\beta)\nu^2\right) \right. \\
&+ \left(-\frac{2}{3}\Gamma_\sigma + \frac{1+3\beta}{2}\nu + \frac{2}{3}k^2\nu p\right)\omega + \frac{2}{3}p\omega^2 \bigg) \\
&+ 3\eta_\mathrm{T} k^2\left(-\frac{2}{3}\Gamma_\sigma + \frac{3}{2}(1+\beta)\nu + p_\sigma k^2\nu - 2k\nu g + \nu\omega^2 \right.\\
&\left.\left. + \omega\left(\frac{2}{3}p + k^2\nu\left(\frac{4}{3}\nu + \zeta\right)\right)\right)\right) + D_{iso}\left(E_\mathrm{T} + \frac{2}{3}k^2\kappa + \omega\right),
\end{aligned}
\tag{20}
$$

where

$$
\begin{aligned}
D_{iso} = \omega^3 &+ \omega^2 k^2\left(\frac{7}{3}\nu + \zeta\right) + \omega\left(1 - 2kg + p_\sigma k^2\right.\\
&\left. + k^4\nu\left(\frac{4}{3}\nu + \zeta\right)\right) + \nu k^2\left(3(1+\beta) - 2kg + k^2 p_\sigma\right).
\end{aligned}
\tag{21}
$$

If we neglect nonlocal contributions to p_σ then $D_{iso} \equiv 0$ is the dispersion relation calculated by Schmit and Tscharnuter (1995) which is contained as the isothermal limit in our model (see also Spahn *et al.* (2000)). Namely, for finite η_T, p_T, Γ_T, and arbitrary but fixed ω and k, the relation $D_{iso} = 0$ follows from the fourth-order, non-isothermal dispersion relation (20) in the limit of infinite heat conductivity κ. This limit is physically clear, since a large heat conductivity rapidly smoothes out fluctuations in the temperature, leading eventually in the mathematical limit

---

[2] Provided that $p_\sigma > 0$, as is the case here, although in an ensemble of dissipatively colliding particles the temperature can in principle be a *decreasing* function of the density (Petzschmann *et al.* 1999).

$\kappa \to \infty$ to the isothermal system from which the dispersion relation $D_{iso} \equiv 0$ is derived. Similarly, the isothermal dispersion relation is obtained for $E_\tau \to \infty$, where E_τ gives the inverse of the relaxation time for a thermally excited system (see Eq. (23) below).

In order to gain insight into basic properties of Eq. (20) we now seek for approximate expressions for its solutions that are valid for large wavelengths. We expand the growth rates $\omega(k)$ in powers of k as

$$\omega(k) = b_0 + b_1 k + b_2 k^2 \ldots . \tag{22}$$

Inserting this relation in Eq. (20) and equating each power of k separately to zero yields four solutions for the b_i, and thus, four approximate solutions $\omega^{(i)}(k)$ which read to order k^2

$$\omega^{(1)}(k) = -E_\tau - k^2 \frac{2}{3}\kappa + k^2 F_1 + O(k^3) \tag{23}$$

$$\omega^{(2)}(k) = i\left[1 - g\,k - \frac{k^2}{2}(g^2 - p_\sigma) + \frac{k^2}{2}F_2\right]$$
$$+ \frac{k^2}{2}\left[\nu\left(\frac{2}{3} + 3\beta\right) - \zeta\right] + \frac{k^2}{2}F_3 + O(k^3) \tag{24}$$

$$\omega^{(3)}(k) = \omega^{(2)*}(k) \tag{25}$$

$$\omega^{(4)}(k) = -3\nu k^2(1+\beta) - 3\frac{\eta_\tau}{E_\tau}\left[\frac{3}{2}\nu(1+\beta) - \frac{2}{3}\Gamma_\sigma\right]k^2 + O(k^3), \tag{26}$$

where

$$F_1 = \frac{p_\tau}{1+E_\tau^2}\left(\frac{2}{3}\Gamma_\sigma - \nu\frac{1+3\beta}{2} + \frac{2}{3}E_\tau p\right) - \frac{3\eta_\tau}{E_\tau(1+E_\tau^2)}$$
$$\times \left(\frac{2}{3}\Gamma_\sigma + \frac{2}{3}E_\tau p - \nu\left\{\frac{3}{2}(1+\beta) + E_\tau^2\right\}\right)$$

$$F_2 = -\frac{p_\tau}{1+E_\tau^2}\left(\frac{2}{3}\Gamma_\sigma E_\tau - \frac{2}{3}p - \nu\frac{1+3\beta}{2}E_\tau\right) + \frac{3\eta_\tau}{1+E_\tau^2}$$
$$\times \left(\frac{2}{3}\Gamma_\sigma + \frac{2}{3}E_\tau p - \nu\frac{1+3\beta}{2}\right)$$

$$F_3 = -\frac{p_\tau}{1+E_\tau^2}\left(\frac{2}{3}\Gamma_\sigma + \frac{2}{3}E_\tau p - \nu\frac{1+3\beta}{2}\right) - \frac{3\eta_\tau}{1+E_\tau^2}$$
$$\times \left(\frac{2}{3}\Gamma_\sigma E_\tau - \frac{2}{3}p - \nu\frac{1+3\beta}{2}E_\tau\right).$$

The mode with purely real growth rate $\omega^{(1)}$ is connected to the thermal stability of the system. The leading wavelength independent term E_τ describes the dependence of the radial energy balance between viscous heating and collisional cooling on variation of the temperature (see Eq. (10)). For stability E_τ has to be positive, requiring the cooling to dominate the heat-

ing when temperature is increased over the ground state value, and vice versa when the temperature is decreased. The second term, proportional to k^2, corresponds to a hydrodynamic heat diffusion mode, with the term $\propto \kappa$ which is purely damping. For the parameter values of the dispersion relation we have determined in simulations in Salo et al. (2001) (see Table III) E_τ is indeed positive in all cases and dominates the other two terms in the expansion $\omega^{(1)}$. Also, we have $\frac{2}{3}\kappa > F_1$. The second and third modes have complex conjugate growth rates $\omega^{(2)}$ and $\omega^{(3)}$ which will give overstability for appropriate β. The terms F_2 and F_3 contain the corrections due to the heat flow equation at this order, the other terms already following from the isothermal model. In the isothermal model the imaginary part of $\omega^{(2)}$ and $\omega^{(3)}$ is the Keplerian frequency with corrections due to self-gravity and pressure forces. The real parts yield an expression for the stability boundary in the the limit $\lambda \to \infty$

$$\beta_{cr}^\infty \equiv \frac{1}{3}\left(\frac{\zeta}{\nu} - \frac{2}{3}\right) \tag{27}$$

so that long wavelengths become overstable if $\beta > \beta_{cr}^\infty$ which was already derived by Schmit and Tscharnuter (1995). A similar criterion was given by Papaloizou and Lin (1988) (Eq. (43) of that paper), which results in Eq. (27) when bulk viscosity is included in their analysis. An exact expression for the line of marginal stability $\beta_{cr}(k)$ for the isothermal model is given in Section 4.2, where eigenfunctions of the hydrodynamic equations are derived at marginal stability. The fourth mode with growth rate $\omega^{(4)}$, corresponding to the viscous instability, is again purely real. It reduces in the isothermal limit to

$$\omega^{(4)} \to -3k^2\nu(1+\beta) + O(k^3) \tag{28}$$

leading to the stability criterion $\beta > -1$ which is equivalent to the conditions derived by Lin and Bodenheimer (1981), and Ward (1981).

Since we introduced with the heat flow an additional diffusion mechanism in the system the terms F_2 and F_3, which are not present in the isothermal case, can be expected to have a primarily stabilizing effect, as we have argued in Spahn et al. (2000). This is confirmed by the quantitative comparison of this study presented in Section 5.

4.2. Eigenfunctions

Here, we determine the overstable eigensolutions of the hydrodynamic model, for simplicity in the isothermal limit, since here the expressions can be given analytically in a compact form. The inclusion of the energy-balance equation leads to no qualitative differences in those properties of the linear eigensolutions which we will eventually compare to simulations, namely the phase differences and amplitude ratios of the perturbations in σ, u, and v. For example, the phase differences in the non-isothermal model, taken in this case from numerically

determined eigenfunctions, yield the same results. However, it is important to note that the stability boundary itself is changed considerably when thermal effects are included.

Restricting our attention again on purely radial modes the matrix (13) reduces in the isothermal limit to

$$\hat{M} = \begin{pmatrix} 0 & -i\,k & 0 \\ i(2g - p_\sigma k) & -k^2\left(\frac{4}{3}\nu + \zeta\right) & 2 \\ -i\frac{3}{2}\nu(1+\beta)k & -1/2 & -k^2\nu \end{pmatrix}, \quad (29)$$

which leads to the third-order dispersion relation given by Eq. (21) and $D_{iso} = 0$. This dispersion relation has two marginal curves in the (λ, β)-plane. The first one, for the purely real eigenvalue, reads

$$\beta_{cr}^{vi}(k) = k\frac{2g - p_\sigma k}{3} - 1, \quad (30)$$

separating the (λ, β)-plane in a region of viscous stability $\beta > \beta_{cr}^{vi}(k)$ and instability $\beta < \beta_{cr}^{vi}(k)$. In the large wavelength limit it reduces to the condition $\beta < 1$ for viscous instability given above. The second marginal curve is for the two oscillatory modes (for long wavelengths given by Eqs. (24) and (25), with $F_2 = F_3 = 0$)

$$\beta_{cr}(k) = \frac{1}{3}\left(\frac{\zeta}{\nu} - \frac{2}{3}\right) + \frac{1}{3}\left(\frac{4}{3} + \frac{\zeta}{\nu}\right)$$

$$\times \left(p_\sigma k^2 - 2gk + \left[\frac{7}{3}\nu + \zeta\right]\nu k^4\right), \quad (31)$$

separating regions of viscous overstability $\beta > \beta_{cr}(k)$ and stability $\beta < \beta_{cr}(k)$.

The two overstable eigenvalues of the matrix $\hat{M}$ at marginal stability $\beta = \beta_{cr}(k)$ are purely imaginary, namely $\pm is$, where

$$s = \sqrt{1 - 2gk + p_\sigma k^2 + \left(\frac{4}{3}\nu + \zeta\right)\nu k^4}. \quad (32)$$

The expression under the root is always positive in the regime of parameter values (g, p_σ, ν) that are of interest here. The corresponding marginal eigenvectors read

$$\varphi_1 = \begin{pmatrix} 2k(i\nu k^2 + s) \\ 2s(i\nu k^2 + s) \\ (\nu k^2 - is)\left(1 + \left[\frac{4}{3}\nu + \zeta\right][\nu k^2 + is]k^2\right) \end{pmatrix} \quad (33)$$

$$\varphi_2 = \begin{pmatrix} 2k(i\nu k^2 - s) \\ -2s(i\nu k^2 - s) \\ (\nu k^2 + is)\left(1 + \left[\frac{4}{3}\nu + \zeta\right][\nu k^2 - is]k^2\right) \end{pmatrix}. \quad (34)$$

Thus, a solution in the overstable subspace to the linear problem at marginal stability reads[3]

$$\begin{pmatrix} \sigma \\ u \\ v \end{pmatrix} = A\,\varphi_1 \exp\{ikx - ist\} + B\,\varphi_2 \exp\{ikx + ist\} + \text{c.c.} \quad (35)$$

For $A = 0$ or $B = 0$ these are left moving or right moving waves

$$\begin{pmatrix} \sigma \\ u \\ v \end{pmatrix}_{L/R} \propto \begin{pmatrix} \mp 2k[s\cos(st \pm kx) + \nu k^2 \sin(st \pm kx)] \\ 2s[s\cos(st \pm kx) + \nu k^2 \sin(st \pm kx)] \\ \cos(st \pm kx)k^2\left[\nu + \left(\frac{4}{3}\nu + \zeta\right)\left(k^4\nu^2 + s^2\right)\right] - s\sin(st \pm kx) \end{pmatrix} \quad (36)$$

and for $A = B$ we obtain the standing wave solution

$$\begin{pmatrix} \sigma \\ u \\ v \end{pmatrix}_S \propto \begin{pmatrix} 2k\sin(kx)[s\sin(st) - \nu k^2 \cos(st)] \\ 2\cos(kx)s[s\cos(st) + \nu k^2 \sin(st)] \\ \cos(kx)\left[\left\{\nu + \left(\frac{4}{3}\nu + \zeta\right)\left(k^4\nu^2 + s^2\right)\right\}k^2\cos(st) - s\sin(st)\right] \end{pmatrix}. \quad (37)$$

In the limit of long wavelengths these solutions yield simple phase shifts in the variables σ, u, v, which are given in Table II. The phase shift between density perturbations and the thermal excitations that are also given in that table have been obtained from a numerical solution of the eigenfunctions of the non-isothermal model.

5. COMPARISON OF THEORY AND SIMULATION

In this section we compare the results of the hydrodynamic model to 3D local N-particle simulations for meter-sized particles at high optical depth ($\tau = 1$ and 2). The simulation box is located at a distance of 100,000 km of a mass point of one saturnian mass. For the inelasticity of the particles we take the standard formula of Bridges *et al.* (1984) for an impact velocity dependent coefficient of restitution. For a description of the simulation method see Salo (1991, 1995).

---

[3] The other eigensolution with growth rate $\omega^{(4)}$ (given approximately by Eq. (28)) will decay rapidly for $\beta = \beta_{cr}(k)$.

TABLE II
Spatial Phase Differences in the Hydrodynamic Model

	Standing wave[a]	Left traveling wave	Right traveling wave
$Ph(\sigma)$-$Ph(u)$	$\pm\frac{\pi}{2}$	π	0
$Ph(\sigma)$-$Ph(v)$	$-\frac{\pi}{2}$	$-\frac{\pi}{2}$	$-\frac{\pi}{2}$
$Ph(v)$-$Ph(u)$	$0, \pi$	$-\frac{\pi}{2}$	$\frac{\pi}{2}$
$Ph(T)$-$Ph(\sigma)$[b]	$\pi, 0$	$-\frac{\pi}{2}$	$\frac{\pi}{2}$

[a] Two given values refer to the respective temporal phase of Eq. (37).

[b] Phase differences for the eigenfunctions of the non-isothermal model have been obtained numerically. They are in agreement with the phase differences of the isothermal eigenfunctions given by Eqs. (36) and (37).

The simulations show overstable behavior when self-gravity is taken into account (Fig. 1). In Salo *et al.* (2001) we demonstrated this for different ways of incorporating self-gravity in the simulations, i.e., full particle–particle gravity interaction and mimicking the effect of gravity with an enhancement of the frequency of vertical oscillations (Wisdom and Tremaine 1988). In both cases we observe similar overstable perturbations in the system, indicating that overstability is not bound to the self-gravity itself but rather to the corresponding changes in the viscous properties of the system. Figure 1 refers to the case of enhanced $\Omega_z = 3.6\Omega$ and $\tau = 1$. Starting from a uniform ground state, the simulated system rapidly develops radial oscillations on a 100-m scale in all the state variables, including the temperature. The maxima in surface density correspond to maxima in the thickness of the system.

In the case of direct particle–particle gravity we observe additionally the occurrence of gravitational wakes, i.e., a nonaxisymmetric structure with characteristic angle of inclination, wavelength, and amplitude. The relative intensity of both types of structure depends for a fixed optical depth on the particle bulk density (Salo *et al.* 2001). As already mentioned in Section 3, the nonlinear non-axisymmetric gravitational wakes are not covered by the analysis of this paper. Consequently, we restrict our attention on simulational systems that consider self-gravity via the enhancement of the vertical frequency, leading to purely radial structure. Also, in this case the system has a stationary ground state, from which transport coefficients and other parameters needed for a comparison to the hydrodynamic model can be obtained, as is described in Salo *et al.* (2001) for different values of the enhancement factor of the frequency of vertical oscillations $\Omega_z/\Omega = 1, 2.0, 3.6$. All the examples in this section refer to the case $\Omega_z/\Omega = 3.6$ if not otherwise stated. An inclusion of direct particle–particle self-gravity, and thus the presence of gravitational wakes, will at least alter the ground state of the system. However, we emphasize, that the growth of radial overstable modes is retained also with full self-gravity (see Salo *et al.* 2001).

5.1. Transport Coefficients

In general, the transport coefficients in the constitutive Eqs. (3) and (4), and the cooling function Γ are functions of the den-

sity, the temperature, and of the dissipativity of the collisions. They can be calculated in the framework of kinetic theory for dense systems, using Enskog's extension of the Boltzmann equation (Chapman and Cowling 1970), to the desired order in the Chapman–Enskog expansion. For granular gases transport coefficients have been derived in the limit of nearly elastic collisions to Navier–Stokes order (see for instance Jenkins and Richman 1985; Lun *et al.* 1984; Garzó and Dufty 1999) and to Burnett order (Sela and Goldhirsch 1998). However, it is known, that, for instance, the dependence of the viscosity on the density and the temperature in a planetary ring (Goldreich and Tremaine 1978a) differs drastically from that in a sheared granular flow. The main reason for this is that the particles in the ring move on curved Keplerian orbits between collisions (Goldreich and Tremaine 1978a). A similar difference cannot be excluded for the other transport processes. Thus, since we want to derive quantitatively
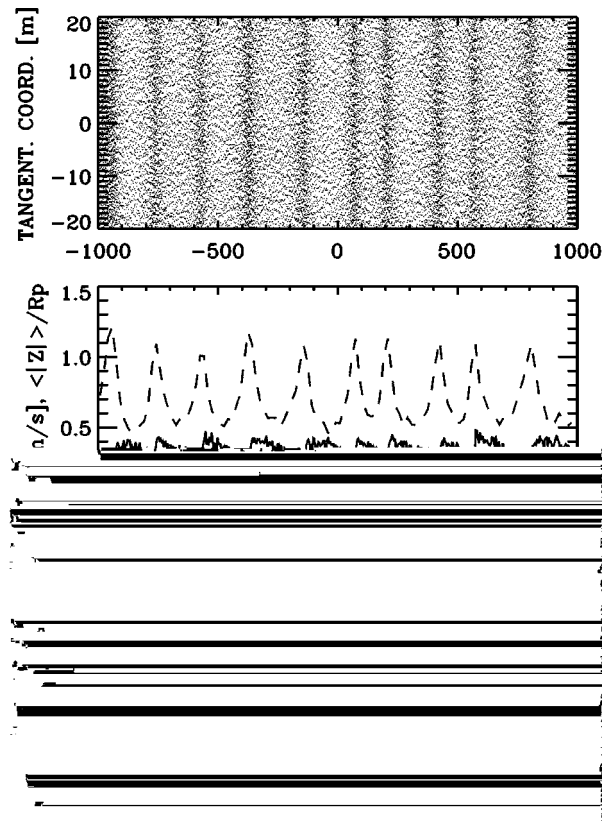

FIG. 1. Perturbations of the state variables due to overstability in a simulation with optical depth $\tau = 1$ and particle-radius 1 m after about 1000 orbital revolutions. The saturnocentric distance was 100,000 km in this simulation and the self-gravity was mimicked by an enhancement of the frequency of vertical oscillations. The upper plot shows the particle-positions projected in the plane $z = 0$ of the simulation box. Here, orbital motion is upward; the planet is to the left. Clearly visible are the radial perturbations on a 100-m length scale due to overstability. The plot in the middle shows the local velocity dispersion (solid line) and $\langle |z| \rangle / R_p$ (dashed line), which is proportional to the local thickness, where R_p is the particle-radius. The lower plot shows the perturbations in the radial velocity (solid) and in the shear corrected tangential velocity (dashed). The phase differences are characteristic for (right) traveling waves (see Table II).

TABLE III
Ground State Parameters[a]

τ	Ω_z/Ω	c [cm/s]	ν	ζ/ν	κ/ν	p^{local}	p_σ	p_T	E_T	η_T	Γ_σ	β
0.5	3.6	0.048	0.348	3.10	6.48	0.411	1.79	1.28	0.72	−0.031	1.34	0.67
1	3.6	0.064	0.357	2.14	4.17	0.160	2.19	1.35	2.50	−0.280	1.74	1.15
1.5	3.6	0.086	0.342	1.99	4.14	0.091	2.41	1.68	3.78	−0.363	1.67	1.19
2	3.6	0.106	0.322	2.12	4.09	0.064	2.72	2.77	4.51	0.378	1.84	1.55
2	1	0.051	0.336	2.13	5.16	0.26	1.85	1.50	1.31	−0.05	1.42	0.87

[a] All the quantities are dimensionless, excluding the effective velocity dispersion c which is given in cm/s. ν is scaled with Ω/c^2, p^{local} with Σc^2, p_σ with c^2, p_T with Σ, E_T with $\Sigma\Omega$, η_T with Σ/Ω, and Γ_σ with Ωc^2. To relate to the figures and tables of Salo *et al.* (2001), velocity dispersion has to be scaled with $R_p\Omega$ and transport coefficients with $R_p^2\Omega$.

the growth rates of perturbations together with the corresponding wavelengths, the granular transport coefficients are too uncertain for our purposes.

In Salo *et al.* (2001) we described the determination of transport coefficients in direct N-body simulations for identical inelastic particles of 1-m radius, the self-gravity approximated by an enhancement of the frequency of vertical oscillations. For the velocity dependent coefficient of restitution the formula

$$\epsilon_n(v_n) = \left(\frac{v_n}{v_B}\right)^{-0.234} \qquad (38)$$

obtained experimentally by Bridges *et al.* (1984) was used. Here, v_n is the normal component of the relative velocity of the impacting particles and $v_B = 0.077$ mm/s. These transport coefficients are used here as values for the parameters of the dispersion relation (20) so that the overstability observed in simulations and in the non-isothermal hydrodynamic model can be compared directly. The relevant parameter sets are displayed in Table III.

All the quantities given in Table III are dimensionless (excluding the effective velocity dispersion c). Time is scaled with the Keplerian frequency, the numerical value we will use is $\Omega = 1.95 \times 10^{-4}$ s^{-1}, the value for a semimajor axis of 100,000 km in the saturnian system. Length is scaled with c/Ω, velocity with c, and density with the ground state density Σ. Thus, the total ground state pressure is unity and the ground state temperature T_0 is equal to p^{local} in this scaling. Note that the numerical value of the ground state density does not alter the analysis in the non-self-gravitating case, or, as in this study, if the effect of self-gravity in the simulations is taken into account by an enhancement of the vertical frequency.

5.2. Initial Growth Rates

In simulations that start from a stationary state we observe the formation of oscillating radial perturbations in the mean surface density, as well as in the non-systematic radial and tangential velocities, and in the velocity dispersion (Fig. 1) (see also Salo *et al.* 2001). We follow the development of the Fourier modes of these perturbations, tabulating them 40 times per orbital period, and observe an initial exponential growth with characteristic times

of a few tens of orbital revolutions, depending on wavelength and optical depth of the run. To facilitate the determination of the growth rates we superimpose a small initial seed to the stationary state in form of low amplitude harmonic perturbations in solely the radial velocity of the simulational system. An example of the measurement of the growth rates from a simulation with optical depth $\tau = 1$ is shown in Fig. 2 on a logarithmic scale. Linear fits yield the growth and decay rates in density and radial and tangential velocity for the different wavelengths. The amplitude in the density perturbation of longer wavelengths may decay initially before the overstable growth sets in, but then the growth rates in all the three state variables are practically the same. The growth rate is positive for all wavelengths larger than a critical wavelength (in the example with $\tau = 1$ about 80 m) and is maximal for an intermediate wavelength (100 m for $\tau = 1$). For modes that are shorter than the critical wavelength we determine the decay rates of the initial seed perturbation which can also be compared to the model predictions. The growing longer modes soon start to excite shorter modes and so the short perturbations start to grow again. This is a nonlinear effect that already sets in shortly after the beginning of the overstable growth.

Using the transport coefficients we have determined in Salo *et al.* (2001) as parameters for the hydrodynamic model we find that the inclusion of the energy balance equation has a stabilizing effect. The boundary for the onset of overstability is shifted to higher optical depth as compared to the isothermal model. In particular, the isothermal model predicts overstability for systems that are found to be stable in simulations. An example with optical depth $\tau = 2$ and $\Omega_z/\Omega = 1.0$ is shown in Fig. 3.

The upper plots show stability diagrams that are obtained from a numerical evaluation of the dispersion relations for the isothermal (left) and the non-isothermal model (right) using the parameters obtained in simulations (Table III). The growth rates corresponding to overstability are the real parts of the two conjugate complex solutions of the dispersion relation. The lower plots display the growth and decay times following from the stability diagrams for the isothermal and non-isothermal case. In quantitative agreement with the direct simulation the non-isothermal model predicts an exponential decay of oscillatory modes of all wavelengths. Generally, for systems without enhancement of the
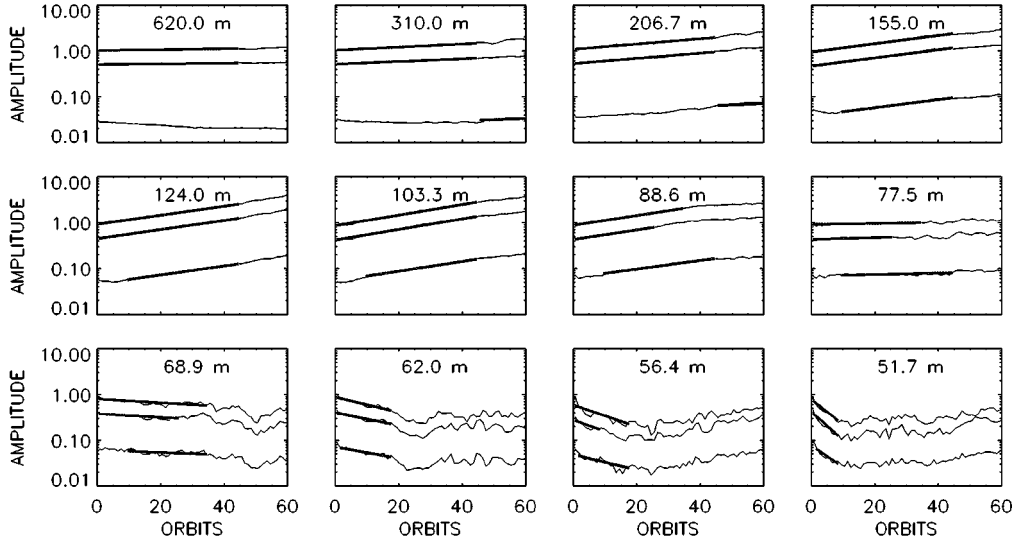
FIG. 2. Example of the measurement of the growth rates from a simulation with optical depth $\tau = 1$. The amplitudes of the Fourier modes of overstable oscillations in the optical depth (lower curve), and the radial (upper curve) and tangential velocity are tabulated 40 times per orbital revolution. Linear fits yield the growth and decay rates for the different modes. The unit of the velocity amplitudes is ΩR_p and the amplitude of the optical depth perturbation is normalized by the ground state optical depth.
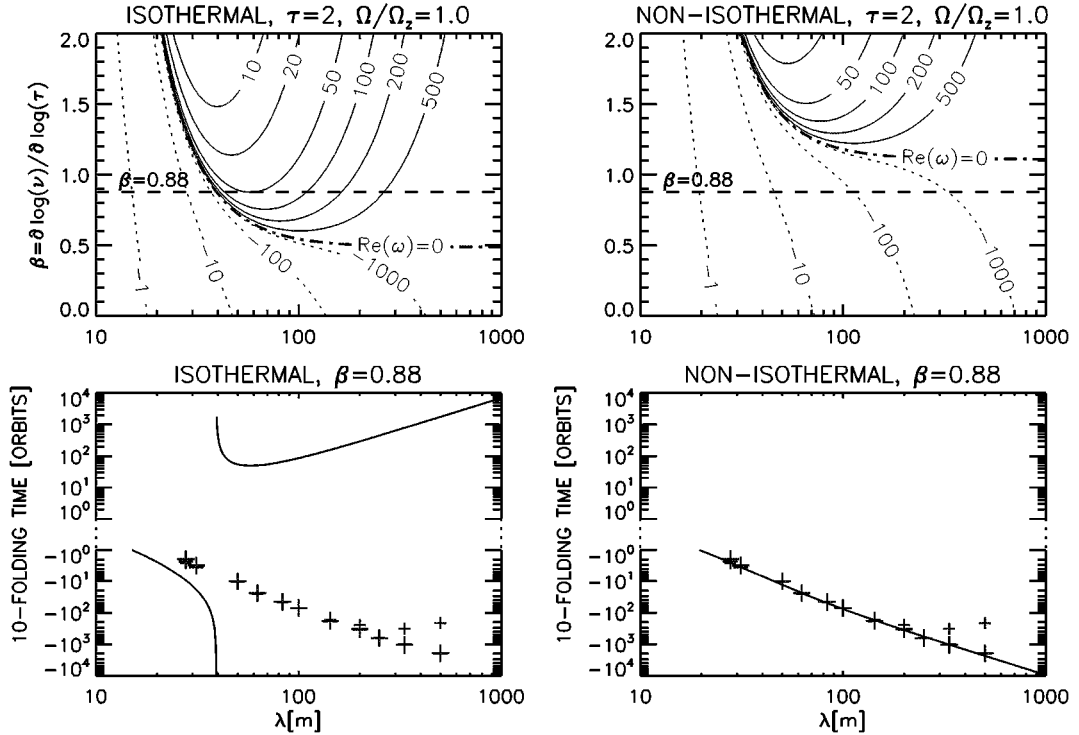
FIG. 3. Upper plots: Lines of equal 10 folding times of radial oscillations in units of orbital revolutions in the (λ, β)-plane. The region above the line of marginal stability (labeled by $Re(\omega) = 0$) is overstable; the region below is stable. This particular case with $\tau = 2$ and without the enhancement of the frequency of vertical oscillations demonstrates the shift of the stability boundary between the isothermal model (left) and the non-isothermal one (right). The horizontal dashed line marks the value of $\beta = 0.88$ for the case $\tau = 2$ and $\Omega_z/\Omega = 1$ as it was determined in simulations (Salo *et al.* 2001). Thus, the isothermal model predicts instability for this system while the non-isothermal model is stable. Lower plots: Results from a simulation with $\tau = 2$ and $\Omega_z/\Omega = 1$ and a radial extension of the simulation box of 2000 m. Small-amplitude radial seed-perturbations of various wavelengths were superposed to the mean values of density and radial and tangential velocity. All wavelengths are found to be stable; the decay times (indicated by negative 10 folding times) are shown in these plots as cross-symbols. The decay times are in good agreement with those predicted by the non-isothermal model while the isothermal model predicts overstable growth of the modes with $\lambda > 40$ m.
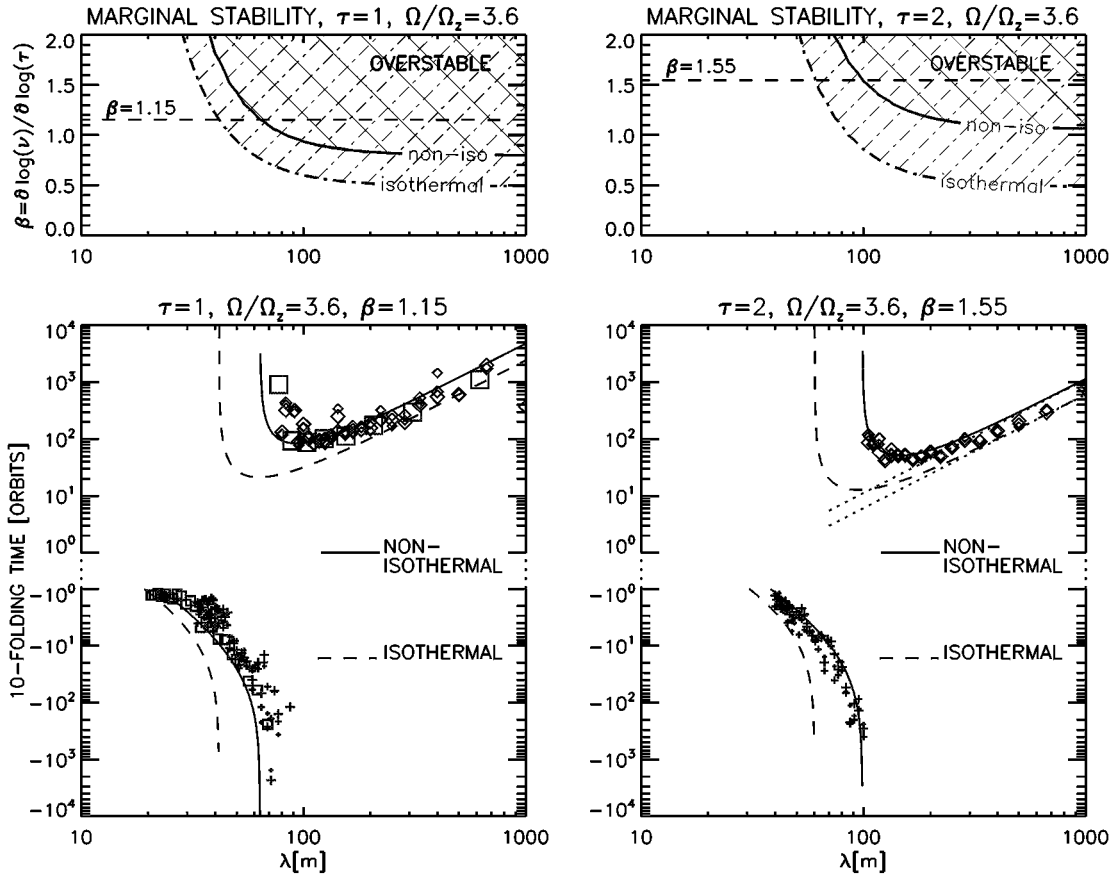
FIG. 4. Upper plots: Lines of marginal stability in the (λ, β)-plane, for systems with $\Omega_z/\Omega = 3.6$ for $\tau = 1$ on the left and for $\tau = 2$ on the right. The dash-dotted line refers to the isothermal case and the solid line to the non-isothermal model. The region above the lines is overstable. The location of the lines of equal 10 folding times relative to the marginal lines is analogous to the upper plots in Fig. 3 The horizontal dashed lines mark the values of β that are relevant for these cases as they were determined in simulations (Salo *et al.* 2001). Thus, for both optical depths both models predict overstability albeit with different growth times and a different wavelength that separates the stable from the unstable region. Lower plots: 10 folding times for theory and simulation in dependence of the wavelength for $\tau = 1$ and $\tau = 2$, $\Omega_z/\Omega = 3.6$. Simulational results are plotted as symbols, diamonds for growth times, crosses for decay times, both from simulations with a radial extension of the simulation box of 2000 m. Different symbol sizes correspond to separately determined growth of perturbations in density (largest), radial velocity, and shear corrected tangential velocity (smallest). The square symbols in the plot for optical depth $\tau = 1$ correspond to growth and decay times from a simulation with a reduced radial extension of 620 m. Also shown is the asymptotic (large λ) value of the rise times in the plot for optical depth $\tau = 2$ as a dotted line, following from the approximation (24).

frequency of vertical oscillations we find stability up to optical depths as high as $\tau = 4$.

In simulations with enhancement of the frequency of vertical oscillations overstability is observed also at lower optical depths. The condition for overstability is roughly given by $\beta > 1$. This corresponds to $\tau > \tau_{crit}$, where τ_{crit} is slightly less then unity for $\Omega_z/\Omega = 3.6$. Results for $\tau = 1$ and $\tau = 2$ are given in Fig. 4. The lines of marginal stability are shown for the non-isothermal and the isothermal models. In the latter case the stabilizing influence of a larger bulk viscosity $\zeta > \nu$ (as well as nonlocal pressure) is contained, in contrast to the similar plot in Schmit and Tscharnuter (1995), where $\zeta = \nu$ was assumed. Basically, all perturbations with wavelength larger than roughly 100 m are found to be overstable for the dense model-rings under consideration (particle-radius 1 m, elasticity law (38)), with a maximum growth rate at a somewhat larger wavelength. The growth rates

decrease for increasing wavelength, finally going to zero for perturbations of a large spatial extension.

In Fig. 4 (lower plots) 10 folding times are shown as predicted by the hydrodynamic model and obtained from simulations. The agreement between simulation and theory is improved when the energy balance equation is considered in the analysis. The diamond symbols in these plots are the growth times obtained from simulations with a radial extension of the simulation box of 2000 m. For $\tau = 1$ growth times from a simulation with reduced radial box-length (620 m) are also shown as square symbols. The growth times are also practically independent of the tangential width of the box except for a slight delay of the onset of the overstable growth in a tangentially larger system.

The frequency intensity of the overstable oscillations for the different modes is shown in Fig. 5 as a contour plot from a
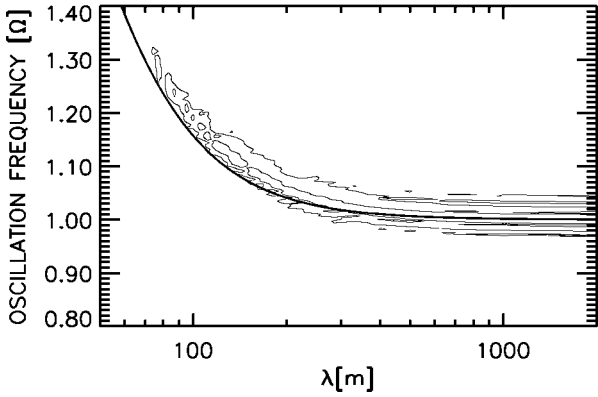
FIG. 5. The frequency intensity (Lomb periodogram) of the overstable oscillations from a simulation with optical depth $\tau = 2$, $\Omega_z/\Omega = 3.6$ as a contour plot in the (ω, λ)-plane. The solid line is the theoretical curve from the numerical solution of the dispersion relation (20).

simulation with $\tau = 2$. The solid line is the is the oscillation frequency predicted by the hydrodynamic model as the imaginary part of the conjugate complex solutions of the dispersion relation Eq. (20). In this case where the self-gravity is approxi-

mated by $\Omega_z/\Omega > 1$ the frequency is always larger than the Keplerian frequency. In a system with true particle–particle gravity the wavelength dependence of the frequency is qualitatively covered by Eq. (32). Ignoring the small ($\propto k^4$) viscosity term, this means that all wavelengths smaller than the Jeans-length

$$\lambda_J = \pi \frac{p_\sigma}{g} \qquad (39)$$

oscillate faster than the Keplerian frequency, and those larger than λ_J oscillate more slowly. The oscillation frequencies for simulations with true particle–particle gravity are shown in Fig. 3 of Salo et al. (2001).

The influence of various parameters on the growth times of the oscillatory instability is shown in Fig. 6 for an example with $\tau = 2$. Interestingly, the 10 folding times of overstable modes suffer a similar shift in the (λ, β)-plane when parameters are varied. An important parameter, already present in the isothermal model, is the bulk viscosity ζ. In many studies that were based on hydrodynamic models it was assumed that the bulk viscosity was equal to the shear viscosity. In the simulational systems we investigated in Salo et al. (2001), it is found to
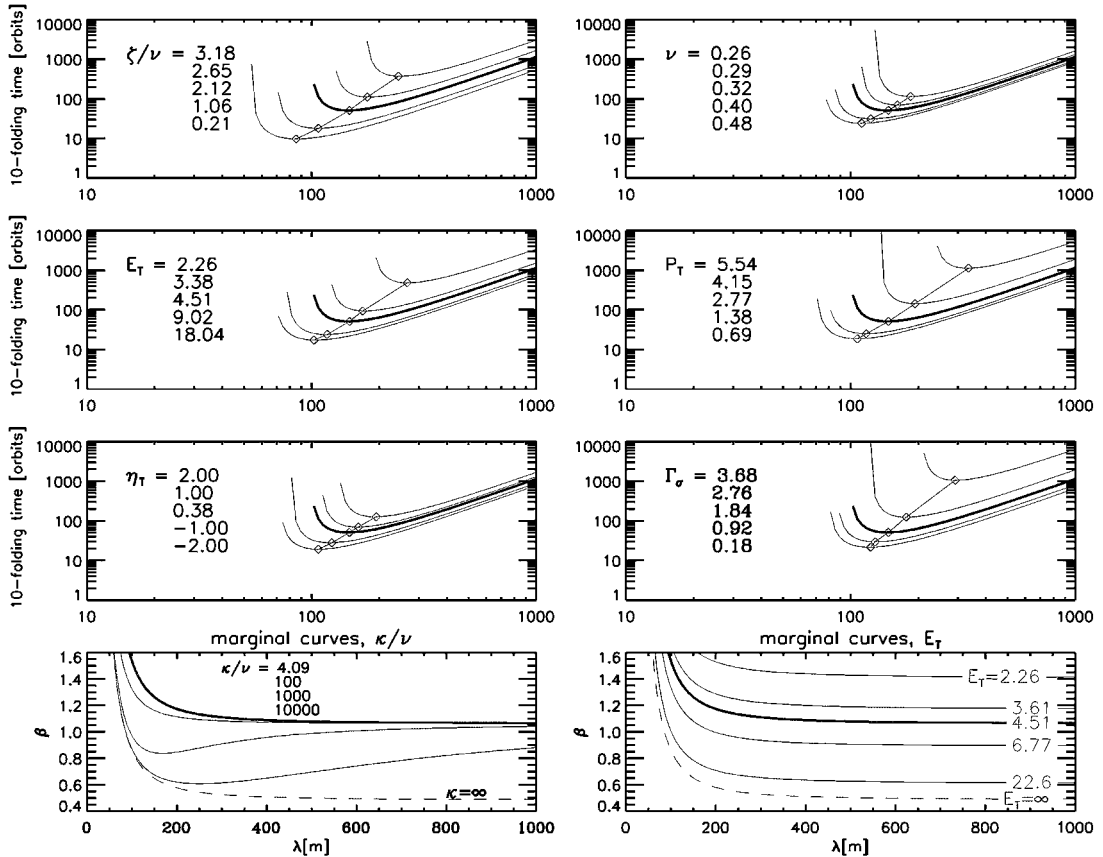

FIG. 6. The influence of a variation of parameters of the model on the growth times of overstable modes of the non-isothermal model for $\tau = 2$. In each plot a single parameter is varied; the others are kept constant. The respective values as they are determined in simulations are represented with a thick line. The last two plots show the convergence of the line of marginal stability toward that of the isothermal model (dashed) in the limit of large heat conductivity or large E_T, respectively.
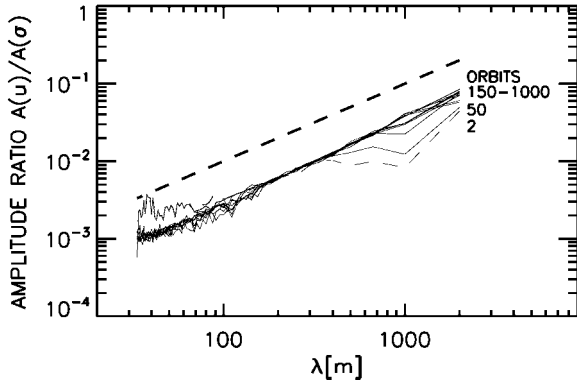
FIG. 7. The ratio of the amplitudes of perturbations in surface density and radial velocity plotted against the wavelength for a simulation with optical depth $\tau = 1$ and $\Omega_z/\Omega = 3.6$. The different lines correspond to different times, starting with the dashed curve. In course of the time development the ratio approaches a linear dependence (compare to thick dashed line) on the wavelength that is predicted by the hydrodynamic model (Eqs. (36) and (37)) for not too short wavelengths. The duration of the record in this plot was about 1000 orbital periods.

be about double the shear viscosity, a shift that stabilizes the system considerably. Other parameters introduced with the energy balance that may have a large influence on the growth times are p_T, η_T, and Γ_σ. The dependence of the growth times on the

(dimensional) wavelength scales with the effective velocity dispersion c.

The ratio of heat conductivity to shear viscosity determined in simulations is about 4–6 for the optical depths that have been investigated in Salo *et al.* (2001). The stability behavior of the hydrodynamic model is insensitive to moderate variations of that parameter, while the effect of the thermal equation itself is large, as can be seen from the shift in the marginal stability line for $\kappa \to \infty$, corresponding to an isothermal model. This large influence can rather be attributed to the relaxation of thermal excitations to a balance of collisional cooling and viscous heating, which is neglected in an isothermal model. The time scale of this relaxation is given by E_T^{-1} (see Eqs. (10) and (23)).

5.3. Eigensolutions

In Section 4.2 we obtained eigensolutions for a simple isothermal hydrodynamic model of the ring's flow. These solutions were computed at the critical value of the parameter β, see Eq. (37), from the eigenvectors of the linear problem that correspond to the overstable eigenvalues. The other eigensolution decays rapidly with characteristic time that is given to leading order in k by the eigenvalue $\omega^{(4)}$ in Eq. (28). In spite of the simplifications made in the derivation of that solution we observe
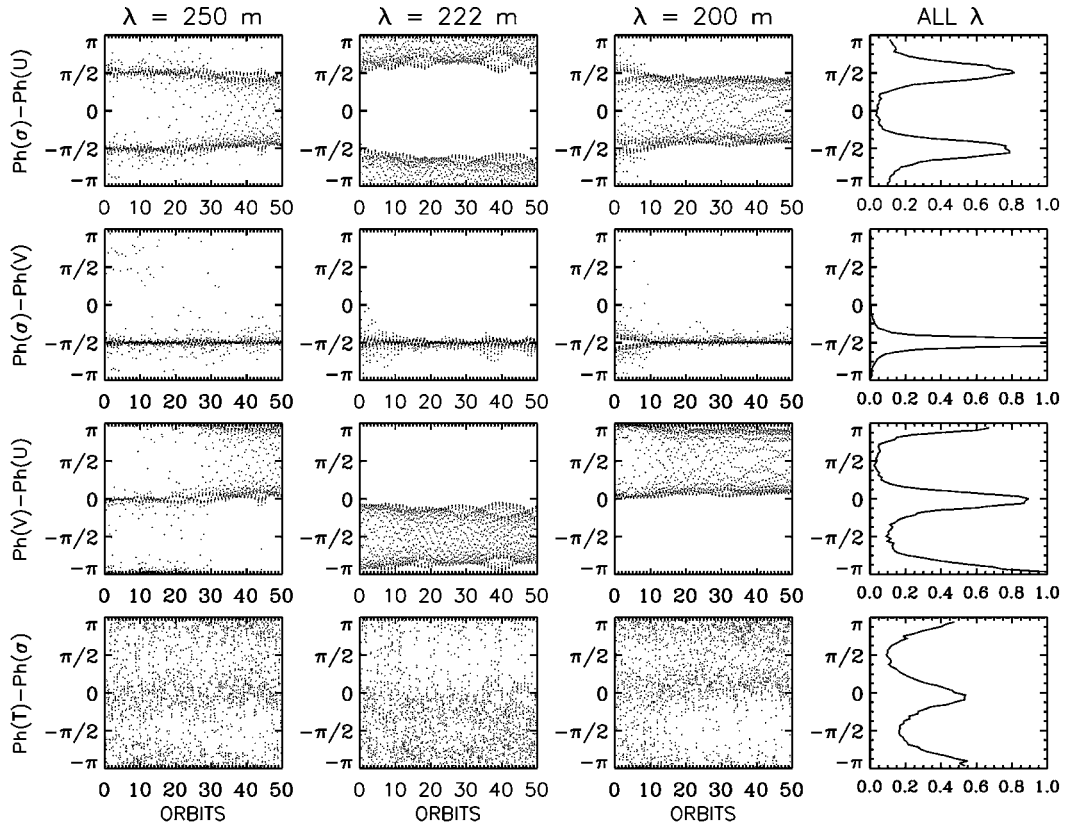

FIG. 8. The phase differences of the state variables σ, u, and v, and T for selected wavelengths are shown (first three columns) from a simulation with $\tau = 1$. They are determined 40 times per orbital revolution for 50 orbital periods. The last column shows the phase differences summed up over all (overstable) wavelengths in a histogram with normalized area. The simulational data points accumulate at the theoretical values given by Eq. (37) for standing waves.

qualitative agreements with the overstable modes in the simulations.

For $k \ll 1$ and thus $s \sim 1$, in the model the ratio of the oscillations of the radial velocity and the shear corrected tangential velocity is about 2 (see Eqs. (36) and (37)), which is also observed approximately in the simulations, as can be seen in Fig. 1. This was also found in a numerical solution of the nonlinear isothermal hydrodynamic equations far from threshold $\beta = \beta_{cr}(k)$ performed by Schmit and Tscharnuter (1999).

For long wavelengths the ratio of the amplitudes of the velocity perturbations to the density amplitude should be proportional to λ (see Eq. (37)). For a simulation we show this ratio in Fig. 7, where the linear dependence inferred from the theory is indeed observed (see also Fig. 2).

Also, we compare the phase differences of the state variables obtained from simulations to those of the hydrodynamic eigensolutions for standing waves and traveling waves. In the linear regime both are equally good solutions. In those runs where the

small initial seed perturbation has been superimposed on the radial velocities we observe in the early stage of the time development phase differences that are consistent with those of the hydrodynamic standing wave solution (37); see Table II. In Fig. 8 these are shown for 50 orbital periods tabulated from a simulation.

The phases of the simulational system accumulate at the theoretically determined values. From the initial seed perturbations in the radial velocity alone the system develops oscillations in all the state variables that keep the characteristic phase differences of the standing wave solution for more than 50 orbital periods. In the following development the system shows intermediate transitions to traveling waves which finally displace the standing wave, as shown in Fig. 9. This transition seems to be connected with the slowing down of the amplitude growth due to the nonlinearity.

In runs without seed perturbations, both standing waves and traveling waves are observed in the linear regime with a much
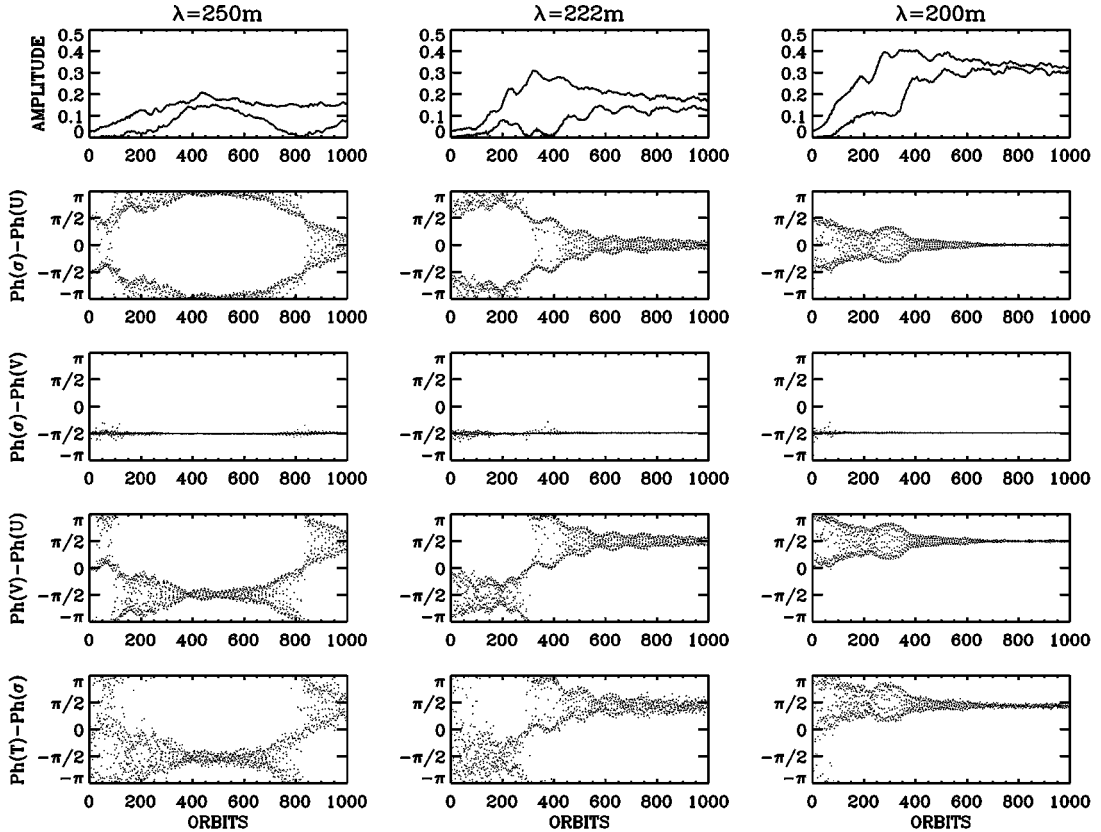

FIG. 9. The long time development of typical modes in a simulation with $\Omega_z/\Omega = 3.6$ and $\tau = 1$. The Fourier amplitudes of perturbations in σ, u, v, and T for three different wavelengths have been tabulated 40 times per orbital revolution. The two curves in the upper plot show the time development of the maxima and minima of the amplitudes of the density perturbation. Only when the system forms a standing wave the minimum Fourier amplitude found in an appropriate time interval (a few times the period of overstable oscillations) is close to zero. The growth of the amplitude slows down and finally saturates after 200–400 orbits. Also shown are the phase differences of the state variables for these wavelengths in course of the run. With growing amplitude, traveling waves seem to be preferred: The phase differences of the mode with 250-m wavelength are consistent with those of a (linear) left moving, traveling wave between orbits 200 and 700, for the 222-m wavelength up to orbit 300. These two wavelengths approach later—and the 200-m wavelength from the beginning—the values for the phase shift of a right moving linear wave (see Table II). This particular simulation develops a right traveling wave. In other simulations left traveling waves are observed: The simulation method, using linearized equations of motion for the particles, is invariant under the inversion $x \rightarrow -x$ and $y \rightarrow -y$ of the radial and tangential coordinate.

more rapid transition to traveling waves only. The traveling waves seem to be the preferred state of the nonlinearly saturated modes. Even in the nonlinear state the simulations show the phase differences of the hydrodynamic eigensolutions (36), i.e., for right traveling waves and left traveling waves, respectively, in spite of the fact that the hydrodynamic solutions are strictly valid only at marginal stability. The phase differences for the respective types of solution of the linear hydrodynamic model are displayed in Table II.

6. DISCUSSION

The hydrodynamic model for a dense planetary ring proposed in this paper, being a generalization of the isothermal model investigated in Schmit and Tscharnuter (1995, 1999), successfully describes the initial development of radial oscillatory modes in direct N-particle simulations. The model yields the correct phase shifts between the state variables, the amplitude ratios, the growth rates, and the oscillation frequencies of the overstable modes. Overstability leads to the formation of a radial structure in the ring, growing exponentially in the linear regime, on a time scale of a few tens of orbital periods. Perturbations with a characteristic length of more than about 100 m are overstable, with a maximum growth rate for a slightly larger wavelength.

For a quantitative agreement with simulations the inclusion of the hydrodynamic heat flow equation in the model is necessary. In particular, an isothermal model would predict oscillatory instability also for non-self-gravitating systems, which is not observed in our simulations even at optical depths as high as $\tau = 4$. Crucial for the onset of overstability is the higher collision frequency in a self-gravitating system compared to a non-self-gravitating one of the same optical depth. Other important factors are the appropriate values for the transport coefficients of the ring's flow, the equation of state, and the cooling function that accounts for the collisional energy loss. These have been determined from simulations in Salo et al. (2001) and are used here as parameters in the hydrodynamic model. In this way the hydrodynamic balance laws provide a satisfactory description of the simulated dense systems.

6.1. Limitations of the Model

In general, hydrodynamic modeling assumes that the velocity dispersion of the system can be described by a scalar value. However, in a planetary ring the diagonal components of the velocity dispersion tensor are unequal in general and its principal axes are not aligned with the radial and tangential directions (Salo et al. 2001). The neglect of this anisotropy becomes more severe for systems of lower density. A better theoretical base for the description of the ring's flow is provided by kinetic theory, and thus, the task of investigating directly the kinetic balance laws for an oscillatory instability should be addressed in future.

In our study the self-gravity of the particle-disk is incorporated in the simulations by an enhancement of the frequency of vertical oscillations which flattens the disk and thus increases the collision frequency. An inclusion of the more realistic direct particle–particle self-gravity leads to a similar enhancement of the collision frequency and overstability is retained in this case, as described in Salo et al. (2001). Direct gravity leads, however, to the formation of non-axisymmetric gravitational wakes which then form an altered spatially inhomogeneous ground state for the ring's flow with different viscous properties. Such systems are nearer to the threshold of overstability for plausible parameters, when compared to the treatment with vertical frequency enhancement. Since in the case of direct, particle–particle self-gravity the marginal curve has a minimum for finite wavelength (see Eq. (31)) it is possible that overstability is then restricted to a band of wavelengths around the wavelength of maximal growth.

Our simulations and the hydrodynamic model deal with a system of uni-sized particles. The question arises how the inclusion of a size distribution would alter the viscous overstability. On the hydrodynamic level this would lead to similar balance laws for the mass density, the mass-averaged velocity, and velocity dispersion, as in the uni-sized case but with modified transport coefficients, cooling function, and equation of state, which would now contain contributions from different particle species. Since the viscous properties of a collisional system are mainly determined by the largest particles, the overstability of a system with size-distribution and a given maximum particle-radius should resemble a system of uni-sized particles of that radius with somewhat lower optical depth. Thus, the growth rates of overstable modes are expected to be smaller. In Fig. 5 of Salo et al. (2001) a simulational example is shown for a system with a differential size-distribution $n(r) = r^{-3}$ (0.5 m < r < 5 m), where overstability is observed, although it requires higher dissipation than in the case of identical particles.

6.2. Implications for Saturn's Rings

The inclusion of the energy-balance equation stabilizes low optical depth rings in our model, in contrast to results of previous isothermal studies (Schmit and Tscharnuter 1995). The criterion for oscillatory instability we find is $\beta \equiv \partial \log \nu / \partial \log \sigma \gtrsim 1$ in accordance with direct local particle-simulations that demonstrate the spontaneous development of overstable oscillations in high optical depth particulate rings. In spite of the stabilizing effect of the energy perturbations our self-gravitating simulations also indicate that the threshold of overstability falls in the midst of the range of plausible B-ring parameters.

This stability boundary is in agreement with the simulations carried out by Mosqueira (1996) who verified that the criterion for viscous overstability in perturbed rings, given by Borderies et al. (1985), is fulfilled for the outer saturnian B-ring ($\tau \sim 1.8$) but not for the uranian ε-ring ($\tau \sim 1$).

Thus, viscous overstability is a promising effect to explain structure formation in Saturn's B-ring. In fact, overstability can directly account for a sub-km structure in the optical depth profile of that ring, showing variability on time scales comparable to the orbital period. This size-range lies well within the resolution limit of the cameras onboard Cassini so that our theoretical

prediction can be verified with the expected images and data of that mission.

Of course the linear theory presented in this paper describes merely the onset of instability and the ranges of parameters for which instability is possible. The actual structure-forming process that follows a linear instability is, however, governed by the nonlinearities of the basic equations. In our simulations the exponential growth in the linear regime begins to slow down and finally saturates after 100–1000 orbital periods. This expresses the growth of the perturbations into the nonlinear regime, supposing that the flow is nonlinearly supercritically stable. The saturation sets in first for the fastest growing wavelength and then gradually for those that grow more slowly and is characterized by an interaction of modes of different wavelengths. In a large system this interaction could lead to the formation of a superimposed modulation of the saturated amplitude of oscillation on a much longer length-scale as the wavelength of maximal growth rate (Schmit and Tscharnuter 1999), resembling the structure actually seen in the B-ring.

ACKNOWLEDGMENTS

REFERENCES

Araki, S., and S. Tremaine 1986. The dynamics of dense particle disks. *Icarus* **65**, 83–109.

Binney, J., and S. Tremaine 1987. *Galactic Dynamics*. Princeton Univ. Press, Princeton, NJ.

Blumenthal, G. R., L. T. Yang, and D. N. C. Lin 1984. On the overstability of axisymmetric oscillations in thin accretion disks. *Astrophys. J.* **287**, 774–784.

Borderies, N., P. Goldreich, and S. Tremaine 1985. A granular flow model for dense planetary rings. *Icarus* **63**, 406–420.

Bridges, F., A. Hatzes, and D. Lin 1984. Structure, stability and evolution of Saturn's rings. *Nature* **309**, 333–338.

Chandrasekhar, S. 1981. *Hydrodynamic and Hydromagnetic Stability*. Dover, New york.

Chapman, S., and T. Cowling 1970. *The Mathematical Theory of Non-Uniform Gases*. Cambridge Univ. Press, Cambridge, UK.

Dubrulle, B., and E. Knobloch 1992. On the local stability of accretion disks. *Astron. Astrophys.* **256**, 673–678.

Durisen, R. H. 1995. An instability in planetary rings due to ballistic transport. *Icarus* **115**, 66–85.

Esposito, L. W., M. Ocallaghan, K. E. Simmons, C. W. Hord, R. A. West, A. L. Lane, R. B. Pomphrey, D. L. Coffeen, and M. Sato 1983a. Voyager photopolarimeter stellar occultation of Saturn's rings. *J. Geophys. Res.* **88**, 8643–8649.

Esposito, L. W., M. Ocallaghan, and R. A. West 1983b. The structure of Saturn's rings—Implications from the Voyager stellar occultation. *Icarus* **56**, 439–452.

Garzó, V., and J. Dufty 1999. Dense fluid transport for inelastic hard spheres. *Phys. Rev. E* **59**, 5895–5911.

Goertz, C. K., and G. Morfill 1988. A new instability of Saturn's rings. *Icarus* **74**, 325–330.

Goldreich, P., and S. Tremaine 1978a. The velocity dispersion in Saturn's rings. *Icarus* **34**, 227–239.

Goldreich, P., and S. Tremaine 1978b. The excitation and evolution of density waves. *Astrophys. J.* **222**, 850–858.

Hénon, M. 1981. A simple model of Saturn's rings. *Nature* **293**, 33–35.

Jenkins, J., and M. Richman 1985. Grad's 13-moment system for a dense gas of inelastic spheres. *Arch. Ration. Mech. Anal.* **87**, 355–377.

Julian, W. H., and Toomre, A. 1966. Non-axisymmetric responses of differentially rotating disks of stars. *Astrophys. J.* **146**, 810–830.

Kato, S. 1978. Pulsational instability of accretion disks to axially symmetric oscillations. *Mon. Not. R. Astron. Soc.* **185**, 629–642.

Lin, D. N. C., and P. Bodenheimer, 1981. On the stability of Saturn's rings. *Astrophys. J.* **248**, L83–L86.

Lissauer, J. J., F. H. Shu, and J. N. Cuzzi, 1981. Moonlets in Saturn's rings. *Nature* **292**, 707–711.

Lukkari, J. 1981. Collisional amplification of density fluctuations in Saturn's rings. *Nature* **292**, 433–435.

Lun, C., S. Savage, D. J. Jeffrey, and N. Chepurniy 1984. Kinetic theories for granular flow: Inelastic particles in Cuette flow and slightly inelastic particles in a general flow field. *J. Fluid Mech.* **140**, 223–256.

Mosqueira, I. 1996. Local simulations of perturbed dense planetary rings. *Icarus* **122**, 128–152.

Papaloizou, J. C. B., and D. N. C. Lin 1988. On the pulsational overstability in narrowly confined viscous rings. *Astrophys. J.* **331**, 838–860.

Petzschmann, O., U. Schwarz, F. Spahn, C. Grebogi, and J. Kurths 1999. Length scales of clustering in granular gases. *Phys. Rev. Lett.* **82**, 4819–4822.

Salo, H. 1991. Numerical simulations of dense collisional systems. *Icarus* **90**, 254–270.

Salo, H. 1992a. Gravitational wakes in Saturn's rings. *Nature* **359**, 619–621.

Salo, H. 1992b. Numerical simulations of dense collisional systems: II. Extended distribution of particle size. *Icarus* **96**, 85–106.

Salo, H. 1995. Simulations of dense planetary rings. III. Self-gravitating identical particles. *Icarus* **117**, 287–312.

Salo, H., J. Schmidt, and F. Spahn 2001. Viscous overstability in Saturn's B-ring. I. Direct simulations and measurement of transport coefficients. *Icarus* **153**, 295–315.

Schmit, U., and W. Tscharnuter 1995. A fluid dynamical treatment of the common action of self-gravitation, collisions, and rotation in Saturn's B-ring. *Icarus* **115**, 304–319.

Schmit, U., and W. Tscharnuter 1999. On the formation of the fine-scale structure in Saturn's B-ring. *Icarus* **138**, 173–187.

Sela, N., and I. Goldhirsch 1998. Hydrodynamic equations for rapid flows of smooth inelastic spheres, to Burnett order. *J. Fluid Mech.* **361**, 41–74.

Smith, B. A., L. Soderblom, R. M. Batson, P. M. Bridges, J.L. Inge, H. Masursky, E. Shoemaker, R. F. Beebe, J. Boyce, G. Briggs, A. Bunker, S. A. Collins, C. Hansen, T. V. Johnson, J. L. Mitchell, R. J. Terrile, A. F. Cook, J. N. Cuzzi, J. B. Pollack, G. E. Danielson, A. P. Ingersoll, M. E. Davies, G. E. Hunt, D. Morrison, T. Owen, C. Sagan, J. Veverka, R. Strom, and V. E. Suomi, 1982. A new look at the Saturn system—The Voyager 2 images. *Science* **215**, 505–537.

Spahn, F., J. Schmidt, O. Petzschmann, and H. Salo 2000. Stability analyses of a Keplerian disk of granular grains: Influence of thermal diffusion. *Icarus* **145**, 657–660.

Spahn, F., and H. Sponholz 1989. Existence of moonlets in Saturn's rings inferred from the optical depth profile. *Nature* **339**, 607–608.

Toomre, A. 1964. On the gravitational stability of a disk of stars. *Astrophys. J.* **139**, 1217–1238.

Ward, W. R. 1981. On the radial structure of Saturn's rings. *Geophys. Res. Lett.* **8**, 641–643.

Wisdom, J., and S. Tremaine, 1988. Local simulations of planetary rings. *Astron. J.* **95**, 925–940.